Journal of Sound and Vibration (2002) **254**(4), 733–762
doi:10.1006/jsvi.2001.4119, available online at http://www.idealibrary.com on IDEAL®

LOW-OSCILLATION COMPLEX WAVELETS

P. S. Addison

Civil Engineering Group, School of the Built Environment, Napier University, Edinburgh, Scotland.
E-mail: p.addison@napier.ac.uk

J. N. Watson

Cardiodigital Ltd, Edinburgh, Scotland

AND

T. Feng

Civil and Construction Engineering Department, UMIST, Manchester, England

(*Received* 30 *May* 2001, *and in final form* 1 *November* 2001)

In this paper we explore the use of two low-oscillation complex wavelets—Mexican hat and Morlet—as powerful feature detection tools for data analysis. These wavelets, which have been largely ignored to date in the scientific literature, allow for a decomposition which is more "temporal than spectral" in wavelet space. This is shown to be useful for the detection of small amplitude, short duration signal features which are masked by much larger fluctuations. Wavelet transform-based methods employing these wavelets (based on both wavelet ridges and modulus maxima) are developed and applied to sonic echo NDT signals used for the analysis of structural elements. A new mobility scalogram and associated reflectogram is defined for analysis of impulse response characteristics of structural elements and a novel signal compression technique is described in which the pertinent signal information is contained within a few modulus maxima coefficients. As an example of its usefulness, the signal compression method is employed as a pre-processor for a neural network classifier. The authors believe that low oscillation complex wavelets have wide applicability to other practical signal analysis problems. Their possible application to two such problems is discussed briefly—the interrogation of arrhythmic ECG signals and the detection and characterization of coherent structures in turbulent flow fields.

1. INTRODUCTION

The wavelet transform (WT) has been found particularly useful for analyzing signals which can best be described as aperiodic, noisy, intermittent, transient and so on. Their ability to localize in both time and frequency in a distinctly different way from the traditional short time Fourier transform (STFT) has spawned a number of sophisticated wavelet-based methods for signal decomposition, manipulation and interrogation.

Analyzing wavelets fall into two general categories: continuous and discrete. The choice of the most appropriate wavelet used in the analysis of engineering problems depends very much on the nature of the data itself. Complex wavelets, such as the Morlet wavelet, are well suited to the free vibrations of plates and beams (e.g., references [1–7]). The temporal records of such vibrations quickly exhibit a high degree of complexity due to both the multiple reflections from the specimen edges and the superposition of multiple wavegroups whose group velocity is frequency dependent. The Morlet wavelet is able to unfold these

0022-460X/02/$35.00

signals in time and frequency allowing for the decoupling of vibration modes. Both discrete (e.g., references [8–11]) and continuous (e.g., references [12–16]) (usually complex) wavelets have been used to monitor rotating machinery such as gears, shafts and bearings. Discrete wavelets are favoured when, for example, a small number of data are required as input to a classifier such as a neural network. Continuous wavelets are favoured when high temporal resolution at all scales and/or phase information is required. Most engineering surface characterization work has used discrete wavelets, whose coefficients are used to provide scale-dependent surface characteristics (e.g., references [17–22]). Often, the coefficients are used to verify the fractal scaling of a surface. Discrete wavelet transforms have also been found particularly useful for signal compression problems in engineering (e.g., references [23–25]). Similar patterns of usage of the various available wavelets can be found in other subject areas including geophysics, fluid mechanics, medicine, finance and so on [26].

This paper concentrates on a specific category of complex continuous wavelets—*low-oscillation complex wavelets*—which until now have received little or no mention of their practical application in the scientific or engineering literature. The archetypal continuous complex wavelet used widely in practice is the standard Morlet wavelet. This is usually specified to have approximately five "significant" sinusoidal oscillations within a Gaussian window. The low-oscillation complex wavelets considered herein are much less oscillatory in the sense that they contain fewer (even single) significant oscillations within the window. It is shown that these wavelets are extremely useful for the analysis of certain data sets where the identification of the temporal location of isolated features within a more oscillatory or noisy background is important. This paper is part tutorial on the background of complex low-oscillation wavelets, setting them in the context of continuous wavelet theory, and part report on their application. The paper is structured as follows: In section 2, two low-oscillation complex wavelets are introduced—the complete Morlet wavelet and the complex Mexican hat. This section also contains background wavelet transform theory and outlines modulus maxima and ridge techniques for use in condensing the information contained in continuous wavelet space. Section 3 introduces the test data used in this study—sonic echo NDT time series—and illustrates the ability of low-oscillation complete Morlet wavelets to localize better signal features associated with structural faults. A mobility scalogram is introduced in section 4 together with modulus maxima (ModMax) filtering to remove both spurious oscillations and noise from the signal. Section 5 considers as an example the use of the mobility scalogram modulus maxima as a suitable pre-processing method for neural network classification. The results of the analysis are discussed in section 6 together with possible applications of these wavelets to other areas.

2. LOW-OSCILLATION COMPLEX WAVELETS

Wavelet transforms differ from the STFT as they allow arbitrarily high localization in time of high-frequency signal features. Wavelets do this by having a variable window width which is related to the scale of observation, this flexibility allows for the isolation of the high-frequency features. In effect, the Heisenberg boxes associated with the analyzing wavelet function change shape in the time–frequency plane becoming tall and thin at high frequencies and short and wide at lower frequencies, whereas the fixed window of the STFT dictates Heisenberg boxes of constant dimensions across the time–frequency plane. Another important distinction between wavelet and Fourier analysis is that wavelet analysis is not limited to using sinusoidal analyzing functions, but rather can employ a large selection of localized waveforms—as long as they satisfy the predefined mathematical criteria described below. In this section, a brief review of the wavelet transform and its defining properties is

presented, then two oscillation complex wavelets are described—the low-oscillation complete Morlet wavelet and the complex Mexican hat wavelet.

2.1. BACKGROUND THEORY

The wavelet transform of a continuous time signal, $x(t)$, is defined as

$$T(a, b) = \frac{1}{\sqrt{a}} \int_{-\infty}^{+\infty} x(t)\psi^*\left(\frac{t-b}{a}\right) \mathrm{d}t \tag{1}$$

where $\psi^*(t)$ is the complex conjugate of the wavelet function $\psi(t)$, a is the dilation parameter of the wavelet and b is the location parameter of the wavelet. In order to be classified as a wavelet, a function must satisfy certain mathematical criteria. These are:

(1) A wavelet must have finite energy,

$$E = \int_{-\infty}^{\infty} |\psi(t)|^2 \, \mathrm{d}t < \infty. \tag{2}$$

(2) If $\hat{\psi}(f)$ is the Fourier transform of $\psi(t)$, i.e.,

$$\hat{\psi}(\omega) = \int_{-\infty}^{\infty} \psi(t) \mathrm{e}^{-\mathrm{i}(\omega)t} \, \mathrm{d}t, \tag{3}$$

then the following condition must hold:

$$C_g = \int_0^{\infty} \frac{|\hat{\psi}(\omega)|^2}{\omega} \mathrm{d}\omega < \infty. \tag{4}$$

This implies that the wavelet has no zero-frequency component, i.e., $\hat{\psi}(0) = 0$, or, to put it another way, it must have a zero mean. Equation (4) is known as the *admissibility condition* and C_g is called the *admissibility constant*. The value of C_g depends on the chosen wavelet.

(3) For complex (or analytic) wavelets, the Fourier transform must both be real and vanish for negative frequencies.

The contribution to the signal energy at the specific a scale and b location is given by the two-dimensional wavelet energy density function known as the scalogram:

$$E(a, b) = |T(a, b)|^2. \tag{5}$$

The total energy in the signal may be found from its wavelet transform as follows:

$$E = \frac{1}{C_g} \int_{-\infty}^{+\infty} \int_0^{\infty} \frac{1}{a^2} |T(a, b)|^2 \, \mathrm{d}a \, \mathrm{d}b \left[= \int_{-\infty}^{+\infty} x(t)^2 \, \mathrm{d}t \right]. \tag{6}$$

The contribution to the total energy distribution contained within the signal at a specific a scale is given by

$$E(a) = \int_{-\infty}^{+\infty} |T(a, b)|^2 \, \mathrm{d}b. \tag{7}$$

This is known as wavelet variance and is used to find dominant scales associated with the signal. It has been used often, for example, in the study of coherent structures found in turbulent fluid flows [27–29]. A wavelet-based power spectral density function can be

derived simply from equation (7), which can be compared directly to its Fourier counterpart, i.e.,

$$P_W(\omega) = \frac{1}{\tau \omega_c C_g} \int_0^\tau |T(\omega, b)|^2 \, \mathrm{d}b, \tag{8}$$

where C_g is the admissibility constant, τ is the total time of the signal (taken long enough to ensure that the pertinent statistics have settled down sufficiently for analysis) and ω_c is a representative frequency of the mother wavelet (defined for scale $a = 1$ and location $b = 0$) such as the bandpass centre, peak frequency, central frequency, etc. Thus, the representative frequency, ω, corresponding to a wavelet of arbitrary scale a is given by $\omega = \omega_c/a$.

Finally, as with the Fourier transform, the original signal may be reconstructed using an inverse transform:

$$x(t) = \frac{1}{C_g} \int_{-\infty}^{\infty} \int_0^\infty \frac{1}{\sqrt{a}} \psi\left(\frac{t-b}{a}\right) T(a, b) \frac{\mathrm{d}a \, \mathrm{d}b}{a^2}. \tag{9}$$

In practice, a fine discretiziation of the continuous wavelet transform is computed where usually the b location is discretized at the sampling interval and the a scale is discretized logarithmically. The a scale discretization is often taken as integer powers of 2, however, when finer resolution is required this is changed to fractional powers of two, known as voices reference [30]. The discretized continuous wavelet transform (CWT) is made distinct from the discrete wavelet transform (DWT) in the literature. In its basic form, the DWT employs a dyadic grid (integer power of two scaling in a and b) and orthonormal wavelet basis functions and exhibits zero redundancy. (Actually, the transform integral remains continuous for the DWT but is determined only on a discretized grid of a scales and b locations. And, in practice, the input signal is treated as an initial wavelet approximation to the underlying continuous signal from which, using a multiresolution algorithm, the wavelet transform and inverse transform can be computed discretely, quickly and without loss of signal information.) Many variants of the DWT exist including, most notably, the maximal overlap DWT which allows a finer, more regular discretization of the signal which, although destroying orthogonality, is useful for some statistical applications reference [31]. In this paper, however, we concern ourselves only with the continuous wavelet transform.

As the wavelet transform given by equation (1) is a convolution of the signal with a wavelet function we can use the convolution theorem to express the integral as a product in Fourier space, i.e.,

$$T(a, b) = \frac{1}{2\pi} \int_{-\infty}^{\infty} \hat{x}(\omega) \, \hat{\psi}^*_{a,b}(\omega) \, \mathrm{d}\omega, \tag{10a}$$

where

$$\hat{\psi}^*_{a,b}(\omega) = \sqrt{a} \hat{\psi}^*(a\omega) \mathrm{e}^{\mathrm{i}\omega b} \tag{10b}$$

is the Fourier spectrum of the analyzing wavelet at scale a and location b. In this way, a fast Fourier transform (FFT) algorithm can be employed in practice to compute the wavelet transform.

A vast amount of information is contained within the continuous wavelet transform $T(a,b)$. This can be condensed considerably by considering only local maxima and minima of the transform. Two definitions of these maxima are commonly used in wavelet analysis practice, these are:

(1) Wavelet *ridges*, defined as

$$\frac{\mathrm{d}(|T(a,b)^2|/a)}{\mathrm{d}a} = 0, \tag{11}$$

which are used for the determination of instantaneous frequencies and amplitudes of signal components references [32–36]. Notice that this definition of a ridge uses the rescaled scalogram $|T(a,b)|^2/a$ as it leads to a simpler analytical solution relating the ridge to the instantaneous frequency when a standard Morlet wavelet is employed as the analyzing wavelet (see section 2.3).

(2) Wavelet *modulus maxima*, defined as

$$\frac{\mathrm{d}|T(a,b)|^2}{\mathrm{d}b} = 0 \tag{12}$$

are used for locating and characterizing singularities in the signal. (Note that equation (12) also includes inflection points with zero gradient. These can be easily removed when implementing the modulus maxima method in practice.) Examples of modulus maxima-based methods in engineering, medicine and the characterization of multifractal signals include those by Roux *et al.* [37], Sahambi *et al.* [38, 39], Li and Loehle [40], Kadambe *et al.* [41], Bruce and Adhami [42], Carmona *et al.* [43], Haase and Lehle [44], and Degaudenzi and Arizmedi [45].

2.2. THE MORLET WAVELET

The complete Morlet wavelet is defined as

$$\psi(t) = \frac{1}{\sqrt[4]{\pi}}(\mathrm{e}^{\mathrm{i}\omega_o t} - \mathrm{e}^{-\omega_o^2/2})\,\mathrm{e}^{-t^2/2}, \tag{13}$$

where ω_o is the central frequency of the mother wavelet. The second term in the brackets is known as the correction term, as it corrects for non-zero mean of the complex sinusoid of the first term. In practice, it becomes negligible for values of $\omega_o > 5$. Previous investigators have concentrated on wavelet transforms with ω_o in the range 5–6, where it can be performed without the correction term since it becomes very small. In this case, the Morlet wavelet becomes

$$\psi(t) = \frac{1}{\sqrt[4]{\pi}}\,\mathrm{e}^{\mathrm{i}\omega_o t}\,\mathrm{e}^{-t^2/2}. \tag{14}$$

This truncated Morlet wavelet is invariably used in the literature and often referred to as simply the *Morlet wavelet*. In this paper we use the name, *standard Morlet wavelet*, for this simplified form and *complete Morlet wavelet*, for the complete form given by equation (13).

The standard Morlet wavelet is simply a complex sinusoid within a Gaussian envelope, where the central frequency, ω_o, in effect determines the number of significant oscillations of the complex sinusoid within the Gaussian window. One can observe this from equation (14) in conjunction with Figure 1(a) and 1(b) which plots the real and imaginary parts of the wavelet for $\omega_o = 2$ and 5 respectively. The complex sinusoidal waveform is contained in the term $\mathrm{e}^{\mathrm{i}\varpi_o t}$ $(= \cos(\varpi_o t) + \mathrm{i}\sin(\varpi_o t))$. The Gaussian envelope $\mathrm{e}^{-t^2/2}$ has unit standard deviation and "confines" both the real and imaginary part of the complex sinusoidal waveform. The imaginary part is phase shifted from the real part by a quarter period. The $1/\sqrt[4]{\pi}$ term is a normalization factor which ensures that the wavelet has unit energy. (Note

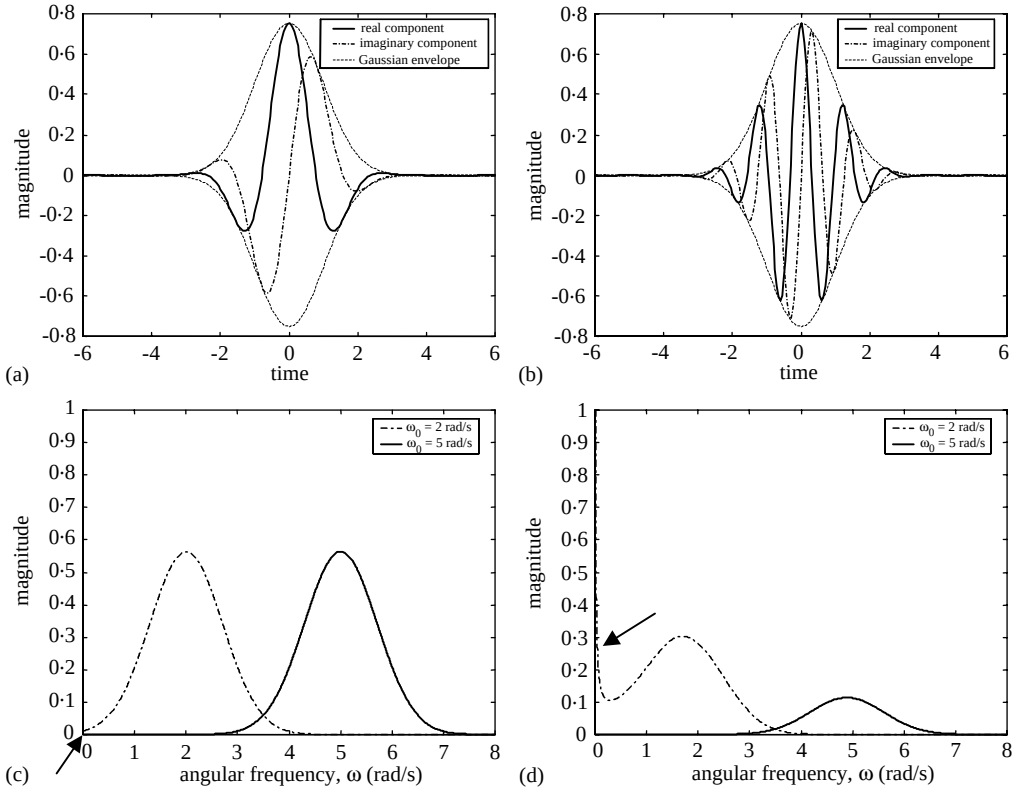

Figure 1. The standard Morlet wavelet at (a) $\omega_0 = 2$, (b) $\omega_0 = 5$, (c) energy spectra $\omega_0 = 2$ and 5, (d) admissibility function $\omega_0 = 2$ and 5.

that various other normalizations are commonplace in the literature each of which require a different C_g to be used to ensure that the original signal and transform contain the same energy.) The complete Morlet wavelet is shown in Figure 2(a) and 2(b), again for $\omega_o = 2$ and 5. If one looks at the waveform carefully, it can be seen that the complex waveform of the complete Morlet wavelet for $\omega_o = 2$ is not completely confined by the Gaussian envelope. This is caused by the correction term, and is also the case for the $\omega_o = 5$ wavelet, but the difference is negligible. For the standard Morlet wavelet, however, the complex sinusoidal waveforms are completely confined by the Gaussian envelope although the wavelet has a non-zero mean. However, again for the $\omega_o = 5$ wavelet this is negligible.

The Fourier transform of the standard Morlet wavelet is

$$\hat{\psi}(\omega) = \sqrt{2}\sqrt[4]{\pi}\, \mathrm{e}^{-(\omega-\omega_o)^2/2} \tag{15}$$

and hence its energy spectrum is

$$|\hat{\psi}(\omega)|^2 = 2\sqrt{\pi}\, \mathrm{e}^{-(\omega-\omega_o)^2}. \tag{16}$$

The energy spectra of the standard Morlet wavelet are shown in Figure 1(c) for both $\omega_o = 2$ and 5. It is obvious from the visual inspection of the plot that the spectrum for $\omega_o = 2$ contains a zero-frequency component (marked by an arrow). For $\omega_o = 5$, the mean component becomes negligible and cannot be observed. The mean component causes a singularity in the admissibility function $|\hat{\psi}(\omega)|^2/\omega$ (cf. equation (4)) as shown in Figure 1(d) (marked by the arrow).

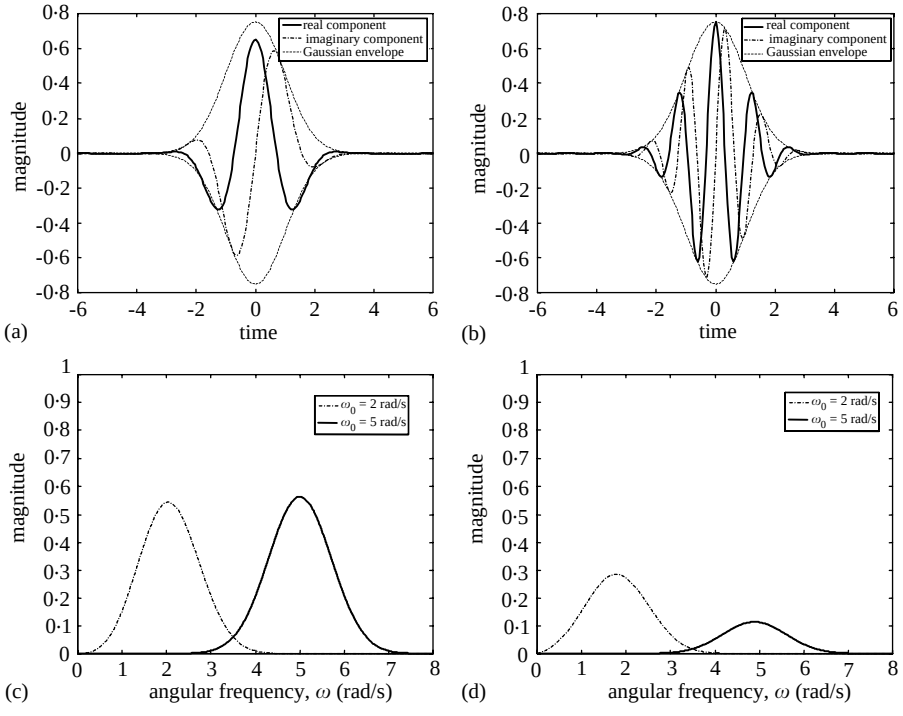

Figure 2. The complete Morlet wavelet at: $\omega_0 = 2$, (b) $\omega_0 = 5$, (c) energy spectra $\omega_0 = 2$ and 5, (d) admissibility function $\omega_0 = 2$ and 5.

The Fourier transform of the complete Morlet wavelet is

$$\hat{\psi}(\omega) = \sqrt{2}\sqrt[4]{\pi}\, e^{-(\omega^2+\omega_o^2)/2}\,(e^{\omega\omega_o} - 1) \tag{17}$$

and its energy spectrum is

$$|\hat{\psi}(\omega)|^2 = 2\sqrt{\pi}\, e^{-(\omega^2+\omega_o^2)}\,(e^{\omega\omega_o} - 1)^2. \tag{18}$$

Figure 2(c) contains the energy spectra for the complete Morlet wavelet transform for both $\omega_o = 2$ and 5. There is no zero-frequency component due to the correction term in the definition of the complete Morlet wavelet hence there is no singularity in the admissibility spectrum (Figure 2(d)). More information on the determination of C_g for both the standard and complete Morlet wavelets is provided in Appendix A.

2.3. WAVELET RIDGE DEFINITION USING STANDARD AND COMPLETE MORLET WAVELET TRANSFORMS

Consider the wavelet transform of a sinusoidal signal given by the complex exponential function

$$x(t) = e^{-i\omega_T t}, \tag{19}$$

where ω_T is the frequency of the sinusoidal waveform. Substituting this into equation (1), the wavelet transform of the signal, $x(t)$, can be shown to be

$$T(a, b) = \sqrt{a}\psi(a\omega_T)e^{-i\omega_T b}, \tag{20}$$

where $\sqrt{a}\psi(a\omega_T)$ is the Fourier transform of the wavelet at scale a. Substituting the Fourier transform of the standard Morlet wavelet (equation (15)) into this equation gives

$$T(a,b) = \sqrt{2}\sqrt[4]{\pi}\sqrt{a}\,\mathrm{e}^{-(a\omega_T-\omega_o)^2/2}\,\mathrm{e}^{-\mathrm{i}\omega_T b}. \tag{21}$$

If one defines the rescaled scalogram as

$$S(a) = |T(a,b)|^2/a = 2\sqrt{\pi}\,\mathrm{e}^{-(a\omega_T-\omega_o)^2}, \tag{22}$$

then differentiating with respect to a gives

$$\frac{\mathrm{d}S}{\mathrm{d}a} = 2\sqrt{\pi}\,\mathrm{e}^{-(a\omega_T-\omega_o)^2}\,[-2\omega_T(a\omega_T-\omega_o)]. \tag{23}$$

Setting $\mathrm{d}S/\mathrm{d}a = 0$ one can see that

$$a_R\omega_T - \omega_o = 0, \tag{24}$$

where a_R is the scale of the ridge maxima. Hence, the instantaneous frequency of the signal can be found from maxima in the rescaled scalogram using the simple expression

$$\omega_T = \frac{\omega_o}{a_R}. \tag{25}$$

If the rescaled scalogram is defined in terms of frequency instead of scale, i.e., $(|T(\omega,b)|^2)/a$ where the "wavelet frequency" ω is related to the scale in terms of the central frequency of the wavelet, i.e., $\omega = \omega_0/a$, then we can see that the instantaneous frequency can be read directly from the spectral location of the ridges in this rescaled scalogram.

Note that by using the standard scalogram, $|T(a,b)|^2$, the instantaneous frequency can be found from the more involved relationship

$$\omega_T = \frac{\omega_o + \sqrt{\omega_0^2+2}}{2a_M}. \tag{26}$$

The determination of an instantaneous frequency from ridges in the rescaled scalogram is described in more detail in reference [32] and for noisy signals by Carmona *et al.* [33, 34]. Ridges have been used by Staszewski [35, 36] in an engineering (dynamics) context within a new procedure for non-linear system identification. In these studies, only the transform values restricted to the ridges, known as the skeleton, were used to reconstruct individually, and hence decouple, the dominant modes of oscillation for use in subsequent damping parameter estimation. The relationship between standard wavelet scalograms and Fourier wavelengths are discussed in reference [46] which provides some brief mathematical detail in Appendix A deriving, essentially, equation (26) in terms of Fourier wavelengths rather than Fourier frequencies. See also Torrence and Compo [47] who provide the information on how to find the Fourier wavelengths for the Morlet, Paul and all the derivatives of Gaussian wavelets (i.e., including the Mexican hat).

Now, we derive a similar expression for ridges of the complete Morlet wavelet, for which we have

$$T(a,b) = \sqrt{2}\sqrt[4]{\pi}\sqrt{a}\,\mathrm{e}^{-(a^2\omega_T^2+\omega_o^2)/2}(\mathrm{e}^{a\omega_T\omega_o}-1)\,\mathrm{e}^{-\mathrm{i}\omega_T b}, \tag{27}$$

hence,

$$S(a) = |T(a,b)|^2/a = 2\sqrt{\pi}\,\mathrm{e}^{-(a^2\omega_T^2+\omega_o^2)}\,(\mathrm{e}^{a\omega_T\omega_o}-1)^2. \tag{28}$$

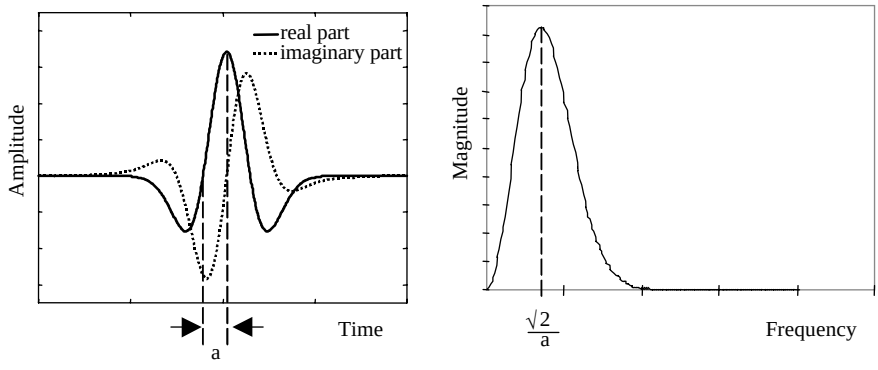

Figure 3. The complex Mexican hat wavelet (left) and its associated frequency spectrum (right). This wavelet has no negative frequency components and has support in the time and frequency domains linked through the dilation parameter a. (The standard, i.e., real only, Mexican hat has its spectral components mirrored in the vertical axis.)

Differentiating gives

$$\frac{\mathrm{d}S}{\mathrm{d}a} = \sqrt[4]{\pi}\, \mathrm{e}^{-(a^2\omega_T^2 + \omega_o^2)} (\mathrm{e}^{a\omega_T\omega_o} - 1)[\omega_o - 2a\omega_T(\mathrm{e}^{a\omega_T\omega_o} - 1)]. \tag{29}$$

Setting $\mathrm{d}S/\mathrm{d}a = 0$ gives

$$a_M = \frac{1}{\omega_o\omega_T} \log\left(1 + \frac{\omega_o}{2a_M\omega_T}\right). \tag{30}$$

Here we see that a more involved computation is required to determine the instantaneous frequency ω_T than for the standard Morlet wavelet transform.

2.4. THE COMPLEX MEXICAN HAT WAVELET

The Mexican hat wavelet is the second derivative of a Gaussian function given by

$$\psi(t) = (1 - t^2)\mathrm{e}^{-t^2/2}. \tag{31}$$

This wavelet has been used, in practice, for a number of data analysis tasks in engineering including the morphological characterization of engineering surfaces [48] and the interrogation of laser-induced ultrasonic signals used to measure stiffness coefficients in a viscoelastic composite material [49]. However, it has been found particularly useful in the analysis of turbulent flows [27, 28, 50–60]. In addition, the Mexican hat is used extensively in studies requiring the use of modulus maxima methods as its maxima lines (and those of other derivatives of Gaussian functions) are guaranteed to be continuous across scales for singularities in the signal [61]. All these studies involve the real-valued Mexican hat function in its one- or two-dimensional form. However, a complex version of the Mexican hat function can easily be constructed by simply setting the negative part of its Fourier frequency spectrum to zero before performing an inverse Fourier transform to obtain the analytic version of the Mexican hat shown in Figure 3. This wavelet has a Gaussian envelope and its transform modulus maxima do not include the side lobe contamination associated with the real-only version.

3. ANALYSIS OF SONIC ECHO PILE DATA

In current practice, the low-strain integrity testing of foundation piles involves the interpretation of a Fourier filtered temporal signal (Sonic Echo Method). This method is widely used as no great pile preparation or excessively expensive equipment is necessary [62]. The technique is an example of impact hammer testing where a pile head's response to an instrumented hammer blow is measured. The resulting time trace is typically made up of transient pulses reflected from structural features of the pile or changes in its surrounding environment. It is often analyzed in conjunction with the spectral response, mobility curve (the transient dynamic response method). In this section, some examples of the wavelet

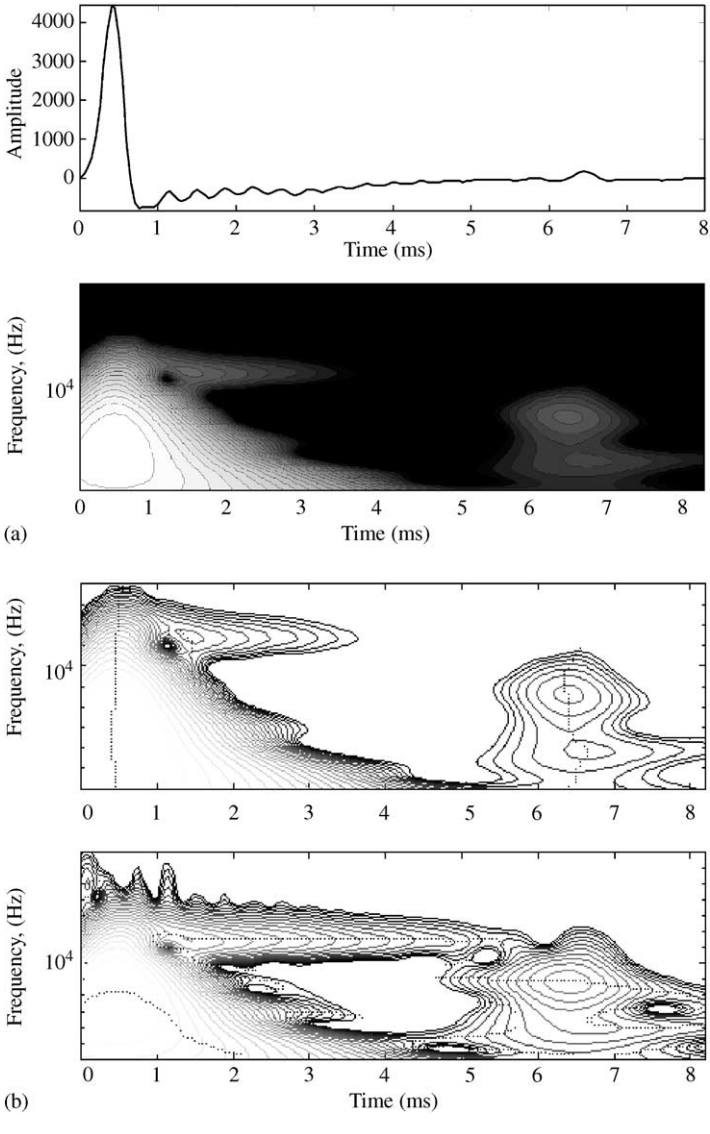

Figure 4. Morlet wavelet transform of sonic echo signal. Complete Morlet wavelet used with ($\omega_0 = 5$): (a) original signal (top) and wavelet transform modulus plot (bottom); (b) modulus maxima plot from scalogram (top) and ridge plots from rescaled scalogram (bottom). (Unfilled contour plots used to aid clarity.)

analysis of sonic echo traces are provided. The analysis is carried out using complete Morlet wavelets on the sonic echo data which is zero padded to eliminate edge effects in the transform space [63]. For the tests considered, the piles are intact and the depth of the pile toe is of specific interest. The location of the toe is found by detecting, from within the signal, the echo reflection from the interface between the bottom of the pile and the surrounding earth. The depth of the toe can then be calculated by knowing the speed of propagation of the stress wave through the pile material.

Figures 4 and 5 contain a finite element generated test signal from a 11 m pile in stiff/very stiff clay for central frequencies $\omega_o = 5$ and 2 respectively. This signal contains three obvious components: the initial pulse, followed immediately by decaying ringdown (lateral

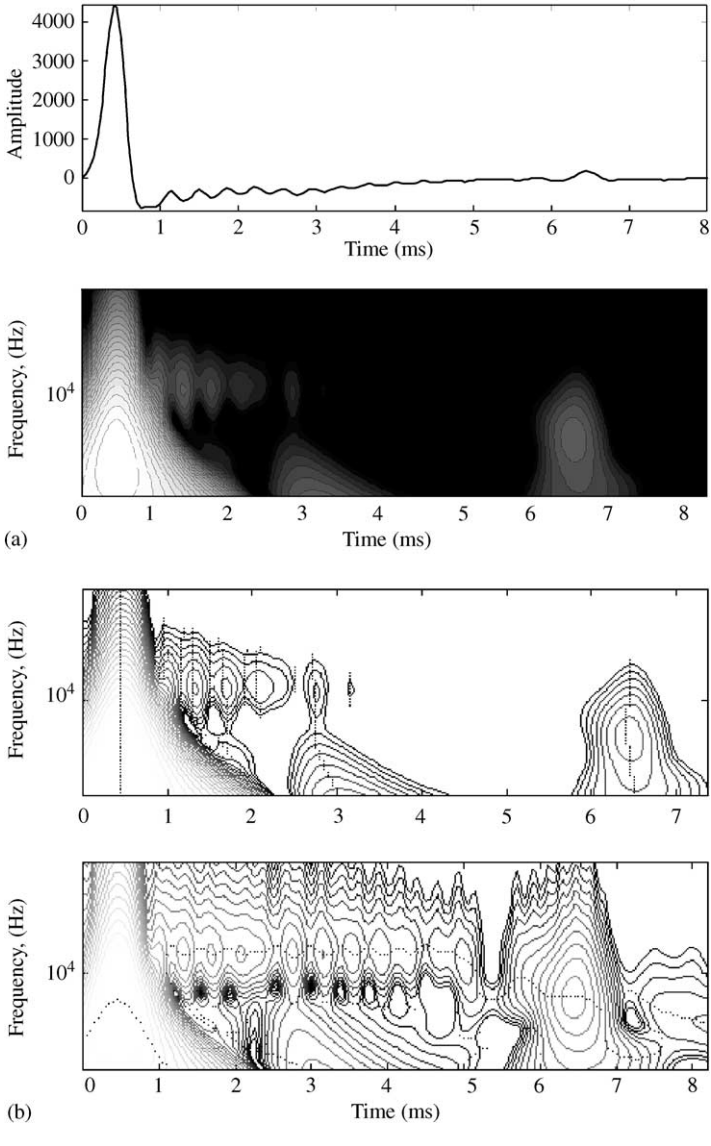

Figure 5. Morlet wavelet transform of sonic echo signal. Complete Morlet wavelet used with ($\omega_0 = 2$): (a) original signal (top) and wavelet transform modulus plot (bottom); (b) modulus maxima plot from scalogram (top) and ridge plots from rescaled scalogram (bottom). (Unfilled contour plots used to aid clarity.)

oscillation of the pile head) and an obvious reflection pulse at about 0·65 ms. The wavelet transform modulus plots, shown below each signal, clearly isolate the reflection pulse in both time and frequency from both the initial pulse and the ringdown oscillations. (Note that in the plot, (1) Hertz rather than radians are used; (2) a logarithmic scale is used for the transform values; and (3) a cut-off has been set to disregard the very low amplitude fluctuations.) The modulus maxima and ridges corresponding to the wavelet transforms are also shown in the figures. Note that the rescaled scalogram $|T(a,b)|^2/a$ is used for the wavelet ridge plot. Very low amplitude fluctuations have been ignored in both plots. One

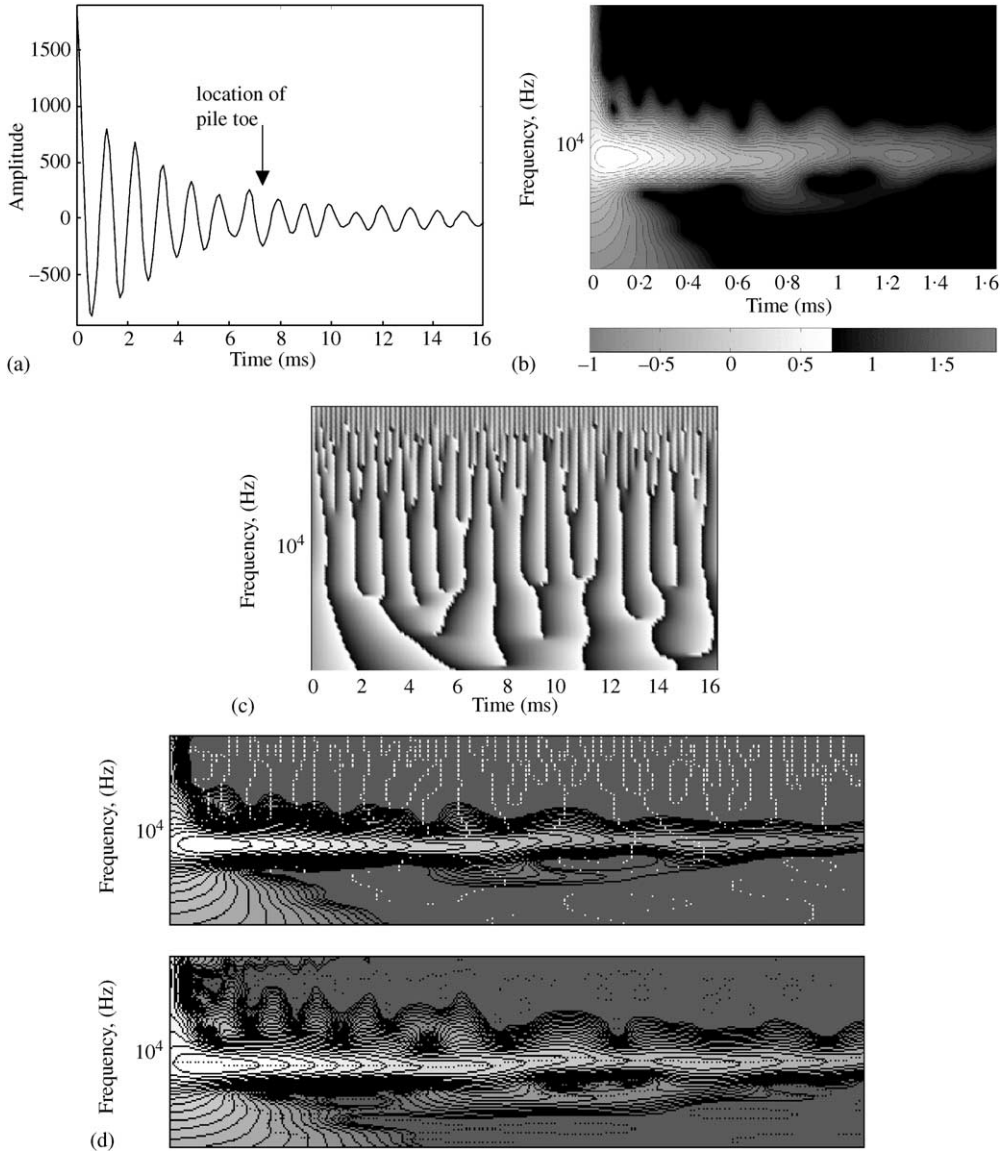

Figure 6. Morlet wavelet transform of sonic echo signal. Complete Morlet wavelet used with ($\omega_0 = 5$): (a) original signal; (b) wavelet transform modulus plot (logarithmic transform scale—white maxima and black minima); (c) wavelet transform phase plot (phase cycles from $-\pi$ (black) to π (white); and (d) plots of modulus maxima (top) and ridges (bottom).

thing that is noticed from the ridge and modulus maxima plots is that the higher central frequency captures more accurately (compactly) the ridge associated with the ringdown, whereas the lower central frequency captures better the temporal location of signal features through the modulus maxima representation.

The signal shown in Figure 6(a) comes from a real 400 mm square pre-cast pile. The pile is installed in 2 m of air, over 2·5 m of gravel, over clay and it is much less clear than the

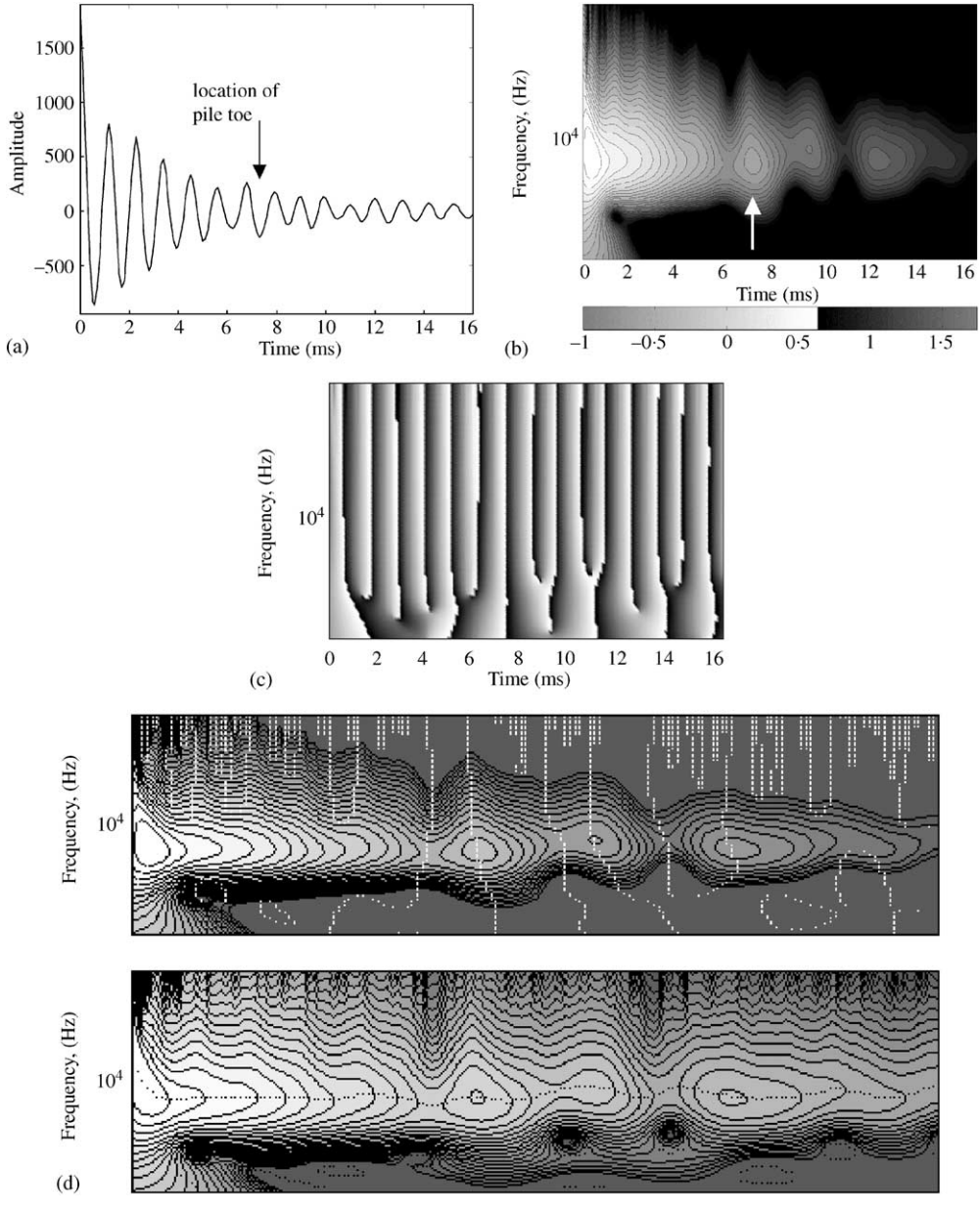

Figure 7. Morlet wavelet transform of sonic echo signal. Complete Morlet wavelet used with ($\omega_0 = 2$): (a) original signal; (b) wavelet transform modulus plot (logarithmic transform scale—white maxima and black minima); (c) Wavelet transform phase plot (phase cycles from $-\pi$ (black) to π (white)); and (d) plots of modulus maxima (top) and ridges (bottom).

previous signal. It is not obvious from visual inspection where the toe reflection is located and, in addition, it cannot be detected using traditional Fourier transform techniques. In this case, we know that the pile length is 12·5 m and hence a reflection from the pile toe is expected to be 7 ms (assuming a propagation velocity $\approx 3500\,\mathrm{ms}^{-1}$) after the initial impulse. This trace is highly oscillatory in nature, with the pile head exhibiting excessive ringdown which masks the reflection information. The wavelet transform scalogram of the pile signal generated using the complete Morlet wavelet with $\omega_o = 5$ is shown in Figure 6(b). This takes the form of a decaying ridge at around the frequency of the ringdown oscillation. This is approximately 9200 Hz. Although the transform has picked up the dominant oscillation well, it contains no useful information regarding the pile toe reflection. The phase plot of the transform is shown in Figure 6(c). The phase plot also gives no indication of the location of the pile toe. The modulus maxima corresponding to the scalogram are shown in the top plot of Figure 6(d). Only two maxima lines cross the ridge, both at locations which do not correspond to the reflection. Numerous maxima lines can be seen at the top of the diagram corresponding to high-frequency, low-amplitude noise in the signal, and a few, very wavy maxima lines can be found at the lower frequencies due to erroneous fluctuations of a very small amplitude. These very low amplitude maxima lines can easily be removed by setting a cut-off as was done in the previous figures. The bottom plot of Figure 6(d) shows the wavelet ridges plotted on the rescaled scalogram.

A similar set of results to Figure 6 is plotted in Figure 7 for the low-oscillation complete Morlet wavelet with $\omega_o = 2$. In this case, an obvious feature is detected in the scalogram (Figure 7(b)) at around 7 ms after the input pulse corresponds to the toe reflection (marked by the arrow in the plot). Although the phase plot shown in Figure 7(c) is much less cluttered due to the less oscillatory nature of the wavelet, again very little can be gained from the phase information. The modulus maxima plot of Figure 7(d) clearly shows a number of maxima lines crossing the ringdown ridge, one passing directly through the reflection feature. Interestingly, the line tracing the dominant ridge is more oscillatory in nature than for the $\omega_o = 5$ wavelet. Figure 8 plots a sequence of wavelet transforms for the signal in Figures 6 and 7. This sequence corresponds to complete Morlet wavelets with ω_o set to 5·5, 4·5, 3·5, 2·5 and 1·5, respectively, from top to bottom. The emergence of the reflection feature in the scalogram with reducing ω_o is obvious in the plot. In fact, the temporal location of the pile toe is only made obvious by employing a low-oscillation wavelet ($\omega_o = 1{\cdot}5$ and 2·5), whereas the standard valued wavelet ($\omega_o = 5{\cdot}5$) cannot detect the feature due to the wavelet smearing the information over more oscillations and hence a larger window width. Note that to produce the same internal analyzing frequency, a larger window is required for the wavelet with larger ω_o—remember ω_o is a parametric constant. This is due to the link between the central frequency and the resulting Heisenberg box dimensions in wavelet space.

Figure 9(a) shows a schematic diagram of a standard valued Morlet wavelet at three different scales and their respective representations in the time–frequency plane, i.e., their associated Heisenberg boxes. σ_ω is the standard deviation of the energy spectrum around the mean spectral components ω_1, ω_2 and ω_3 shown in the figure and σ_t is the corresponding deviations in the temporal energy spectra. Note that the short-term Fourier transform has Heisenberg boxes which have the same dimensions in the time–frequency plane and hence cannot resolve particularly high-frequency components in time nor low-frequency components in frequency. Figure 9(a) shows the effect of changing a while maintaining ω_o constant, and is well known in the literature. Figure 9(b), however, shows the effect of changing ω_o of the mother wavelet. In the figure, Heisenberg boxes in the time–frequency plane for a mother wavelet with three different central frequencies set to a low, medium and high values are depicted. The confining Gaussian windows are all of the

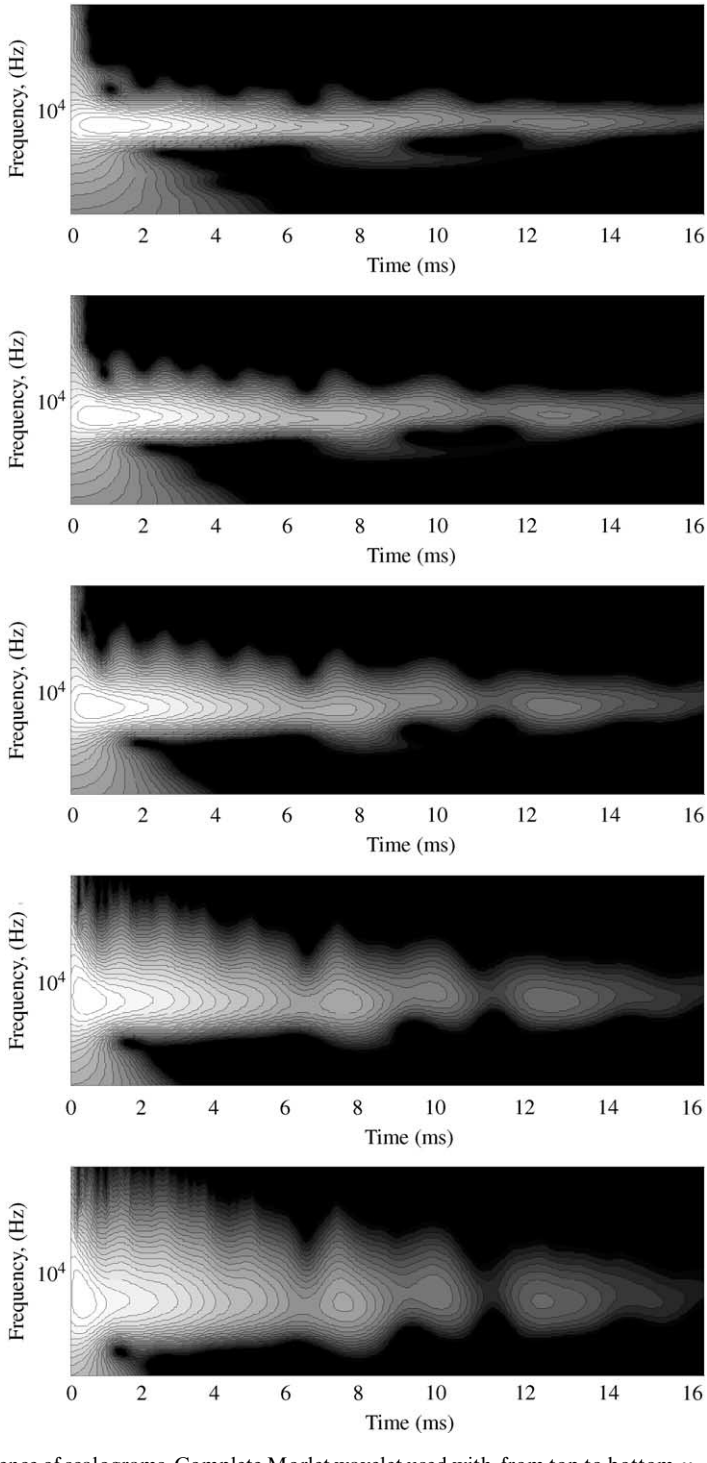

Figure 8. Sequence of scalograms. Complete Morlet wavelet used with, from top to bottom $\omega_0 = 5{\cdot}5, 4{\cdot}5, 3{\cdot}5, 2{\cdot}5$ and $1{\cdot}5$.

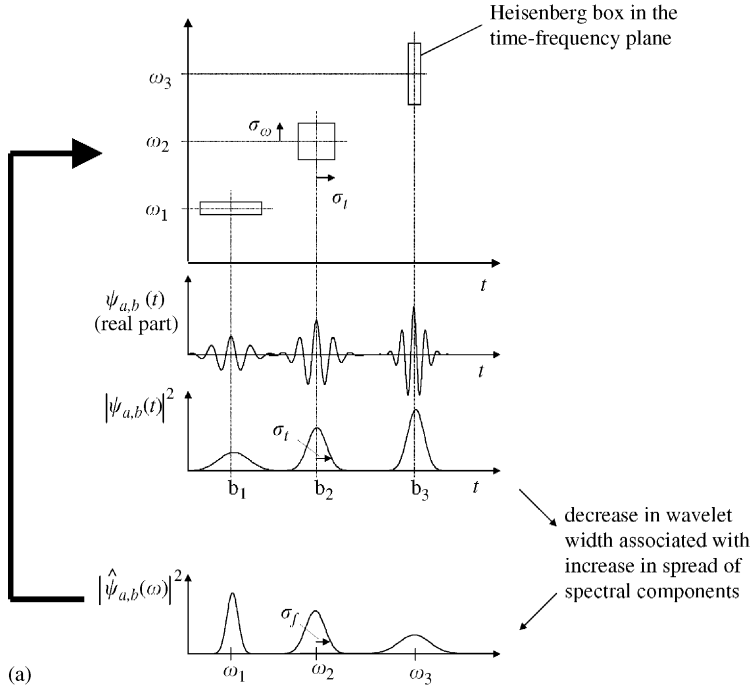

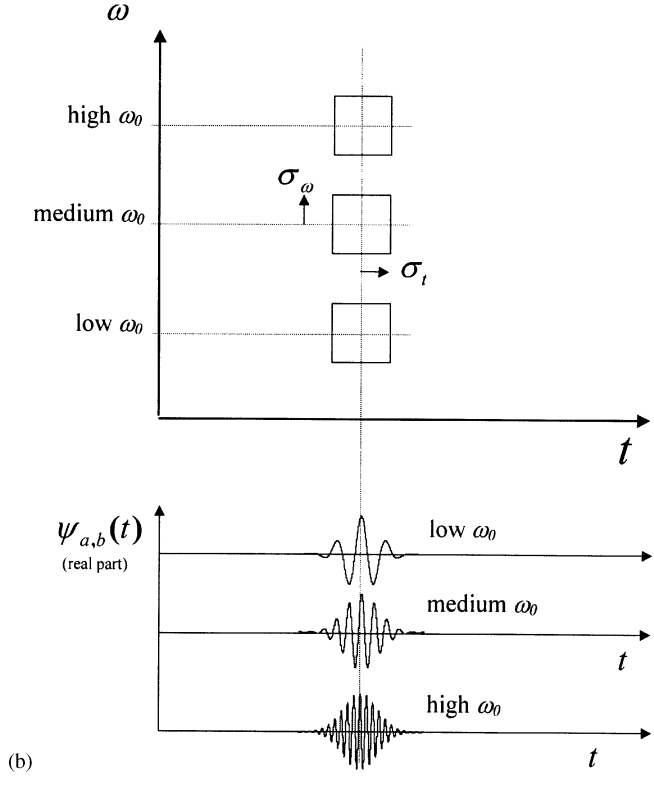

Figure 9. Heisenberg boxes for the complete Morlet wavelet: (a) Heisenberg boxes in the time-frequency plane for a wavelet at various scales; (b) Heisenberg boxes in the time-frequency plane for a mother wavelet with three different central frequencies.

same dimensions. Notice that altering the central frequency of the mother wavelet simply shifts the associated "mother" Heisenberg box up and down the time–frequency plane without altering the box dimensions. This mother Heisenberg box then defines the relative shapes of all the others in the time–frequency plane associated with each wavelet, i.e., the pattern shown in Figure 9(a) is simply shifted up or down the plane.

4. THE MOBILITY SCALOGRAM, MODULUS MAXIMA TEMPORAL FILTERING

The mobility, or mechanical admittance, is a technique commonly used in the analysis of structural test signals. Specifically, it can be described as the frequency response function (FRF) of the system with respect to velocity, that is,

$$H(\omega) = \frac{V(\omega)}{F(\omega)}, \tag{32}$$

where $V(\omega)$ is the spectrum of the velocity time trace and $F(\omega)$ is the spectrum of the input force. Often in modal analysis, the direct calculation of the mobility spectrum is inappropriate due to the presence of noise. However, in pile analysis the spectrum above 1500 Hz is rarely considered and the coherence of the spectrum below this value is sufficiently high for the direct calculation of the mobility spectrum. The inverse Fourier transform of $H(\omega)$ gives the impulse response function which is often referred to as the reflectogram in the literature. It is the basis for wave-tracing techniques because, as with its frequency-domain equivalent, its shape is approximately input magnitude independent. An example of a mobility curve and the corresponding reflectogram is shown in Figure 10 for an 11·5 m cast *in situ* pile with a Fourier cut-off frequency of 1000 Hz employed. The cut-off frequency is necessarily low due to the spectral shape of the Gaussian-like input pulse ($F(\omega)$ in equation (32)). The magnitude of the spectral components above this frequency is often very small causing large peaks in the mobility spectrum.

Now, we present a new concept in wavelet analysis—the *mobility scalogram* [64]. As previously described, the notion of wavelet analysis can be summarized as the convolution of an analytical function of multiple dilations with the signal under investigation. As such, the calculation of the wavelet coefficients for a given scale can be more efficiently calculated in the frequency domain where the wavelet function becomes, effectively, a band pass filter. Hence, for a given scale, or wavelet dilation, the coefficients can be obtained from the inverse Fourier transform of the product of the signal spectrum with the wavelet spectrum at that dilation (equations 10(a) and (b)), thus,

$$T(a, b) = \frac{\sqrt{a}}{2\pi} \int_{-\infty}^{+\infty} \hat{V}(\omega)\hat{\psi}^*(a\omega)\mathrm{e}^{\mathrm{i}\omega b}\mathrm{d}\omega, \tag{33}$$

where a is the wavelet dilation value, $\hat{\psi}^*(\omega)$ the wavelet function spectrum with the superscript "*" representing the complex conjugate and $\hat{V}(\omega)$ is the Fourier transform of the velocity response. However, if one replaces the spectrum of the velocity signal $\hat{V}(\omega)$ in the above equation with that of the mobility curve $\hat{H}^*(\omega)$, the resulting scalogram then becomes, effectively, the wavelet transform of the reflectogram and hence becomes input magnitude, and shape, independent. This scalogram has, therefore, been labelled the *mobility scalogram* by the authors. The mobility scalogram is constructed using wavelets which themselves have a broad range of spectral components, this effectively smoothes the mobility curve—the smoothing function being dependant upon the wavelet used. By employing a wavelet which is similar in shape to the features being sought (the complex

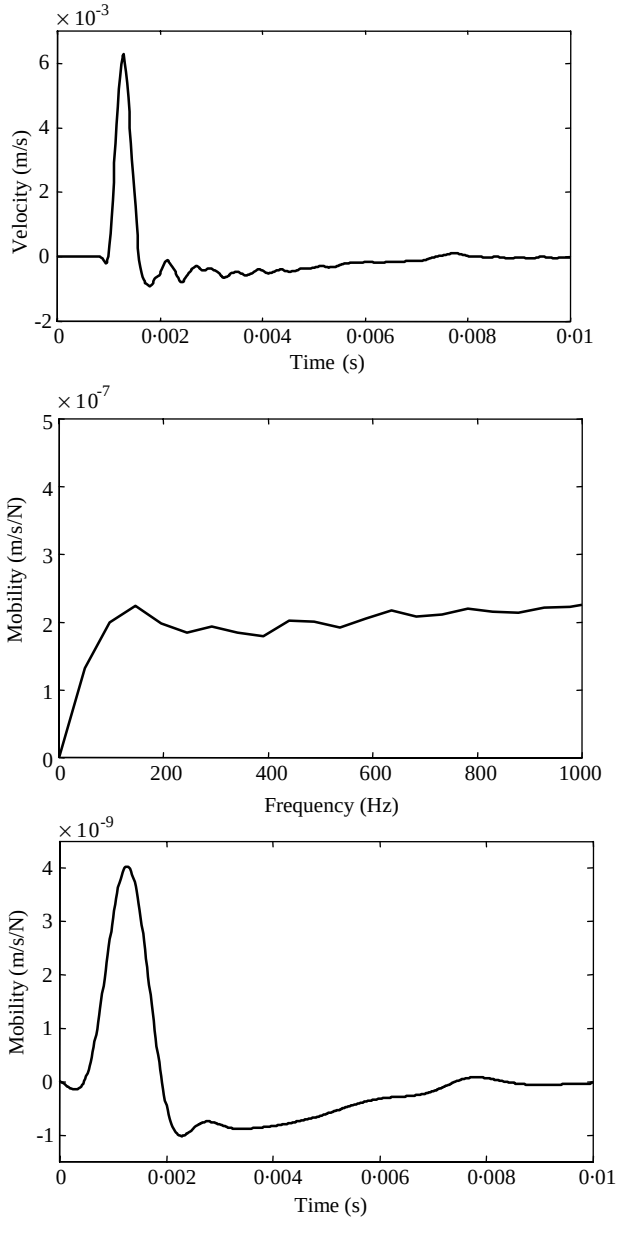

Figure 10. The velocity trace for pile 1, top, its mobility curve beneath, and the reconstructed reflectogram, bottom. The mobility curve has been truncated at 1000 Hz, hence the smoother nature of the reflectogram.

Mexican hat has a Gaussian envelope) the effect is to include high-frequency components only where there are associated low-frequency ones. Hence, using the mobility scalogram is advantageous over the traditional mobility curve which can cause spurious singularities in the high-frequency range and, therefore, spurious oscillations in the reconstructed reflectogram.

The top two plots of Figure 11 contain, respectively, a test signal plus a mobility scalogram constructed as described above using a complex Mexican hat wavelet. Beneath

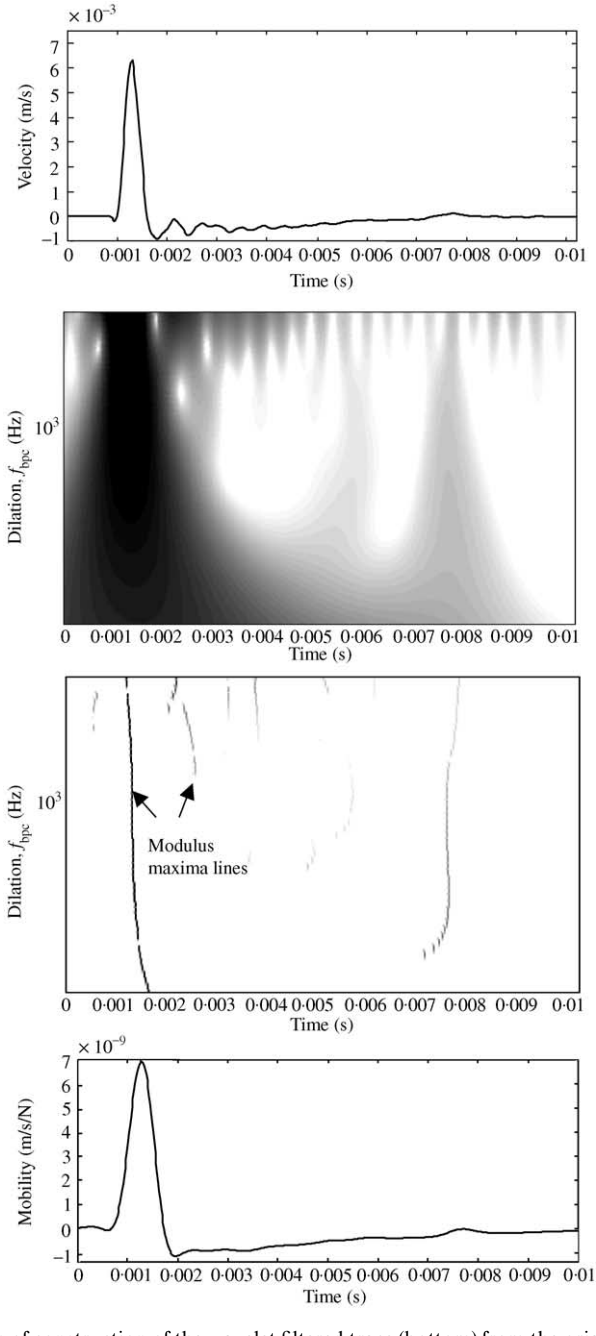

Figure 11. The stages of construction of the wavelet filtered trace (bottom) from the original trace (top) through utilizing the mobility scalogram and modulus maxima techniques.

these is the modulus maxima plot of the scalogram and the wavelet filtered trace. Using the mobility scalogram, temporal denoising has been applied through the implementation of the modulus maxima-based method. Here, the energy in the scalogram is redistributed to its maximal modulus turning points with respect to each scale [65]. By following these

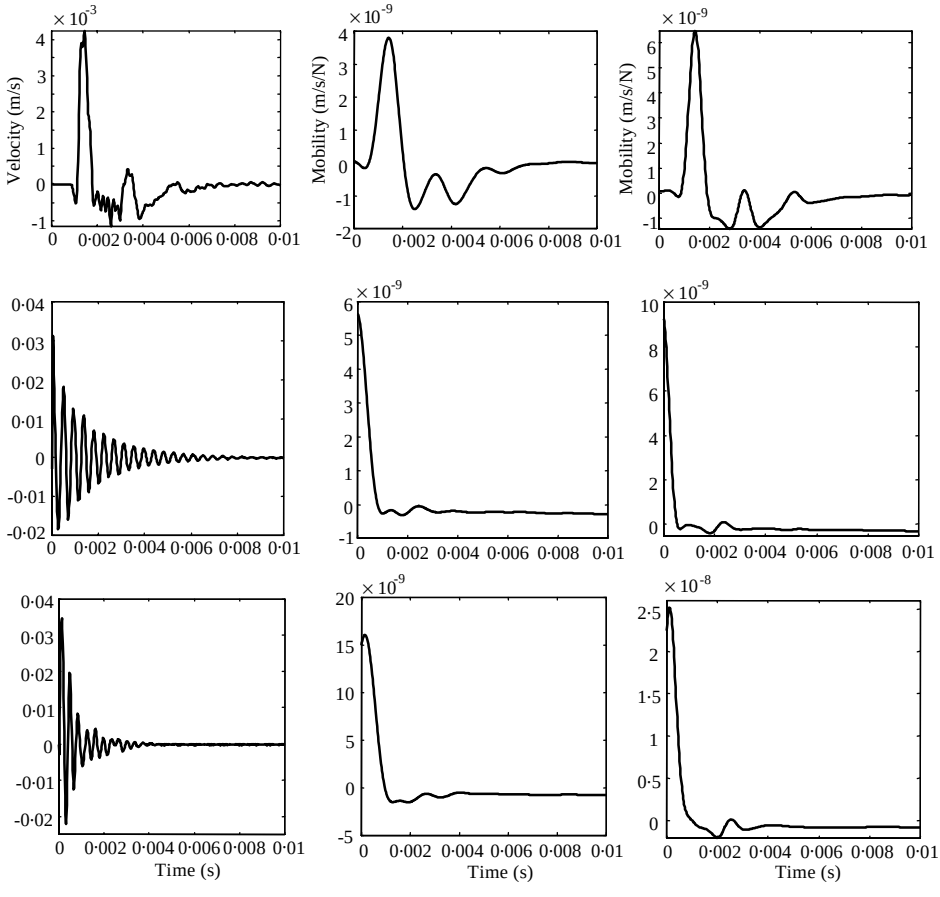

Figure 12. Superior filtering obtained using the mobility scalogram. The initial unfiltered data for the three installed foundation piles are shown in the left-hand column. The filtered traces using the traditional mobility curve are shown in the centre column while that using the mobility scalogram is shown in the right column.

contours from lower frequency scales up to the high-frequency scales one can differentiate the high-frequency components caused by ringdown from those of the reflected echoes and input pulse, i.e., those components with associated lower frequency terms. The method is superior to denoising methods previously proposed by the authors which were based on simply setting a cut-off threshold in the scalogram [66]. The use of this technique also drastically reduces the number of non-zero terms in the presented scalogram. Consequently, this method is useful for the encoding of trace information.

Figure 12 contains the wavelet-filtered signals for three test piles reconstructed using this modulus maxima-based method and their Fourier-based reflectogram equivalents. It can be seen from the figure that, while the amplitude of the trace features are of the order of those of the corresponding Fourier-based reflectograms, their shapes better represent those of the original traces. This is due to the retention of salient high-frequency components while the high-frequency noise has been eradicated. The more accurate representation of the original signal has very obvious advantages, especially when, in practice, an attempt is made to draw inferences from the amplitude and shape of pulse reflections, as in the example of section 5, below.

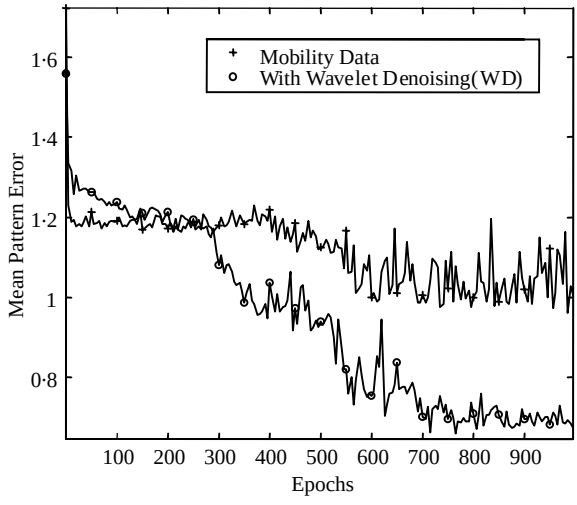

Figure 13. The test set convergence curves for two identical neural networks. One with the normal mobility curve and one with wavelet mobility data. An improved performance of the wavelet filtered data can be noticed.

5. NEURAL NETWORK CLASSIFICATION OF PRE-PROCESSED STRUCTURAL TEST DATA

In the preceding sections we have argued for the employment, in certain cases, of low-oscillation wavelets and introduced the concept of the mobility scalogram. For the example given, the structural testing of installed foundation piles, the advantage in having filtered data that better represents the original trace in shape is clear. The amplitudes and morphology of the returning pulses in the sonic echo trace are representative of the degree and position of faults in the installed pile. To illustrate this point a multi-layered neural network has been trained using conventional back-propagation techniques to compute a pile's cross-sectional profile from its sonic echo trace. A comparison between the similarities of the two sets of input patterns was made up of: (1) the conventional Fourier-based mobility curves and (2) the Fourier transforms of the wavelet-filtered impulse response traces (e.g., the FFTs of the centre and right-hand traces of Figure 12). The network topology could then be identical for the two data sets, the input space of the same size and the maximum frequency presented (band pass centre in the wavelet case) that was the same for both. The learning parameters were, however, optimized for each network individually through parametric studies.

The networks were trained using numerically generated, finite element traces of piles of similar design in similar soil conditions to those described above. The convergence curves of the respective networks are shown in Figure 13 and the final network errors are presented in Table 1. An improved performance of the network presented with the wavelet pre-processed data can be noticed. The wavelet method has allowed for a better encapsulation of the original trace information, thus improving the eventual network performance. Indeed, although the networks were trained on numerically generated data when traces from similar, real, installed piles are presented to the wavelet pre-processed network significant faults can be identified—see, for examples, Figure 14.

TABLE 1

Comparison of wavelet and fourier test data pre-processing for neural network interpretation

	Mean pattern error	
	Training set	Test set
Wavelet mobility data	0·49 ± 0·04	0·66 ± 0·05
FFT mobility data	0·94 ± 0·05	1·07 ± 0·49

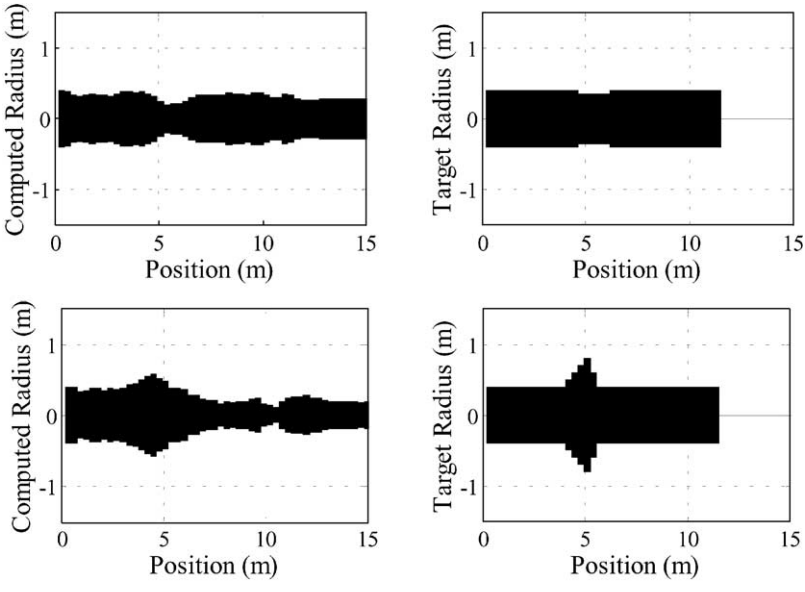

Figure 14. An illustration of the ability of the neural network trained on wavelet-filtered data to deduce faults in real installed piles even when trained on numerically generated data. On the right is the design profile of the installed pile; on the left is the profile calculated by the network.

6. DISCUSSION AND CONCLUSIONS

In this paper we have attempted to bring low-oscillation complex wavelets to the attention of the applied scientist. As far as we are aware, these new (although "forgotten" or "ignored" might be better adjectives) wavelets are not currently being used in practice, although we believe that they have much to offer. The early part of the paper is explanatory in nature, taking time to cover the basic theory of these wavelets and plotting them in the time and frequency domains. We have then illustrated their use in practice, highlighting their advantages over decompositions using wavelets of a more oscillatory nature.

Morlet wavelets with low values of ω_o contain only a few significant oscillations within the Gaussian window. We have shown that this improves the location detection capabilities of the wavelet transform (see especially Figure 8). The same is true of the complex Mexican hat wavelet. The most commonly used complex wavelet in practice, the standard Morlet wavelet with $\omega_o \geqslant 5$, is more oscillatory and allows for a better resolution of frequency components. For the complete Morlet wavelet, the relationship between the central

frequency of the wavelet and its spectral–temporal location characteristics can be explained through the consideration of the shapes of the Heisenberg boxes in the wavelet domain (Figures 9(a) and 9(b)). The ridge of the complete Morlet wavelet corresponding to the instantaneous frequency of a signal has been defined in terms of its central frequency. In addition, the computation of the admissibility constant C_g for both the complete and standard Morlet wavelets has been discussed (Appendix A).

The advantage of the wavelet transform over either a pure spectral or temporal decomposition of the signal is that the pertinent signals features can be characterized in the time–frequency plane. This allows them to be separated from other features occurring at similar times or having a similar frequency make-up. The signal decomposition is more "temporal than spectral" for low-oscillation complex wavelets. The best wavelet to chose (e.g., the most appropriate central frequency if using a complete Morlet) depends very much upon the precise spectral–temporal characteristics of the features sought. Note, however, that at very low values of central frequency the real part of the complete Morlet wavelet, which includes the correction term, behaves as a Mexican hat wavelet and the complex part begins to dominate. This is shown in Appendix B.

A new analysis tool, the *mobility scalogram* has been described, where the corresponding reflectogram, generated using only the modulus maxima, has shown itself to be better than Fourier methods at retaining the high-frequency components associated with signal features. The retention of this high-frequency information leads to a reconstruction which better represents the shape of the pertinent signal features. In addition, the method requires very few components from the modulus maxima to be used in the reconstruction thus providing a useful data analysis tool, for example, in the pre-processing of signals prior to the input in a classifier. Actually, this method is recommended over discrete wavelet methods which are translation invariant and hence can often fail to capture the signal features succinctly.

Although this paper has used low-oscillation complex wavelets to examine sonic echo velocity traces from piled foundations, it is envisaged that they will be useful in the interrogation of a wide variety of other signals. Two examples of particular interest to the authors are mentioned briefly. It is first suggested that the temporal location characteristics of the low-oscillation Morlet wavelet will prove useful in the examination of a variety of medical signals, a particular case in point is the arrhythmic ECG signal which contains both high-frequency spiking and lower frequency modulations mixed with external interferences such as mains noise and muscle artefact [67, 68]. The preliminary research work, by two of the authors (PSA, JNW), found the evidence for this to be true for a particular category of common arrhythmia. It is also suggested that the complex Mexican hat and/or the low-oscillation Morlet wavelet could prove particularly useful in the analysis of turbulent flows. Using these wavelets would both remove the side-lobe contamination associated with the real-valued Mexican hat as well as provide phase information in the studies of coherent flow structures. (In fact, the authors find it rather surprising that, as far as they are aware, the complex Mexican hat has not yet been used in such studies.) This wavelet should be particularly good at the location (temporal in 1-D signals and spatial in 2-D fields) of coherent flow structures. The spectral decomposition of flow fields has a long history in fluid dynamics. However, the decomposition of velocity or vorticity fields using a 2-D low-oscillation complex wavelet would generate a complex decomposition which is more "temporal than spectral". Thus, it is suggested that, this would be better to identify and provide phase information on isolated flow features of short duration and/or limited spatial extent containing a broad band of frequency components.

The main conclusion from the work is that both the complete Morlet wavelet with the tuneable central frequency, ω_o, extending down to very low values and the complex

Mexican hat wavelet provide better defined phase information and enhanced temporal isolation of signal components. These low-oscillation complex wavelets offer a powerful feature detection tool for a variety of data analysis tasks. As far as the authors are aware, these wavelets appear to have been overlooked in the literature and it is suggested that the analysis of many data sets would benefit from a re-examination using continuous low-oscillation wavelets.

ACKNOWLEDGMENTS

This research work was partly funded by EPSRC grant GR/M21881. The authors would like to acknowledge Mike Kightley and Richard Nicholson of TESTAL Ltd and Stephen Kemp of TECHNOTRADE Ltd for their useful input to the NDT data analysis work. In addition, TESTCONSULT Ltd, is thanked for kindly providing additional EPSRC test data.

REFERENCES

1. T. Önsay and A. G. Haddow 1994 *Journal of the Acoustical Society of America* **95**, 1441–1449. Wavelet transform analysis of transient wave propagation in a dispersive medium.
2. K. Kishimoto, H. Inoue, M. Hamada and T. Shibuya 1995 *Transactions of the American Society of Mechanical Engineers, Journal of Applied Mechanics* **62**, 841–846. Time frequency analysis of dispersive waves by means of wavelet transform.
3. H. Inoue, K. Kishimoto and T. Shibuya 1996 *Experimental Mechanics* **36**, 212–217. Experimental wavelet analysis of flexural waves in beams.
4. L. Gaul and S. Hurlebaus 1997 *Mechanical Systems and Signal Processing* **12**, 783–795. Identification of the impact location on a plate using wavelets.
5. H. Jeong and Y.-S. Jang 2000 *Composite Structures* **49**, 443–450. Wavelet analysis of plate wave propagation in composite laminates.
6. D. E. Newland 1999 *Transactions of the American Society of Mechanical Engineers, Journal of Vibrations and Acoustics* **121**, 149–155. Ridge and phase identification in the frequency analysis of transient signals by harmonic wavelets.
7. D. E. Newland 1999 *Philosophical Transactions of the Royal Society* **357**, 2607–2625. Harmonic wavelets in vibrations and acoustics.
8. B. A. Paya, I. I. Esat and M. N. M. Badi 1997 *Mechanical Systems and Signal Processing* **11**, 751–765. Artificial neural network based fault diagnostics of rotating machinery using wavelet transforms as a preprocessor.
9. N. Aretakis and K. Mathioudakis 1997 *Transactions of the American Society of Mechanical Engineers, Journal of Engineering for Gas Turbines and Power* **119**, 870–876. Wavelet analysis for gas turbine fault diagnostics.
10. J. Piñeyro, A. Klempnow and V. Lescano 2000 *Journal of Alloys and Compounds* **310**, 276–279. Effectiveness of new spectral tools in the anomaly detection of roller element bearings.
11. K. Shibata, A. Takahashi and T. Shirai 2000 *Mechanical Systems and Signal Processing* **14**, 229–241. Fault diagnosis of rotating machinery through visualisation of sound signals.
12. W. J. Staszewski and G. R. Tomlinson 1994 *Mechanical Systems and Signal Processing* **8**, 289–307. Application of the wavelet transform to fault detection in a spur gear.
13. A. Yoshida, Y. Ohue and H. Ishikawa 2000 *Tribology International* **33**, 273–279. Diagnosis of tooth surface failure by wavelet transform of dynamic characteristics.
14. W. J. Wang and P. D. Mcfadden 1996 *Journal of Sound and Vibration* **192**, 927–939. Application wavelets gearbox vibration signals for fault detection.
15. D. Boulahbal, M. Farid Golnaraghi and F. Ismail 1999 *Mechanical Systems and Signal Processing* **13**, 423–436. Amplitude and phase wavelet maps for the detection of cracks in geared systems.
16. J. Lin and L. Qu 2000 *Journal of Sound and Vibration* **243**, 135–148. Feature extraction based on Morlet wavelet and its application for mechanical fault diagnosis.

17. X. Q. JIANG, L. BLUNT and K. J. STOUT 1999 *Proceedings of the Institution of Mechanical Engineers, Part H, Journal of Engineering in Medicine* **213**, 49–68. Three-dimensional surface characterisation for orthopaedic joint protheses.
18. X. Q. JIANG, L. BLUNT and K. J. STOUT 2000 *Proceedings of the Royal Society of London A* **456**, 2283–2313. A lifting wavelet representation for surface characterization.
19. I. SIMONSEN, A. HANSEN and O. M. NES 1998 *Physical Review E* **58**, 2779–2787. Determination of the hurst exponent by use of wavelet transforms.
20. G. N. FRANTZISKONIS, L. B. SIMON, J. WOO and T. E. MATIKAS 2000 *European Journal of Mechanics A/Solids* **19**, 309–318. Multiscale characterisation of pitting corrosion and application to an aluminium alloy.
21. R. S. SRINIVASAN and K. L. WOOD 1997 *Transactions of the American Society of Mechanical Engineers, Journal of Mechanical Design* **119**, 185–193. A form tolerancing theory using fractals and wavelets.
22. I. Y. TUMER, R. S. SRINIVASAN and K. L. WOOD 1995 *Journal of Manufacturing Systems* **14**, 378–392. Investigation of characteristic measures for the analysis and synthesis of precision-machined surfaces.
23. W. J. STASZEWSKI 1998 *Journal of Sound and Vibration* **211**, 735–760. Wavelet based compression and feature selection for vibration analysis.
24. M. TANAKA, M. SAKAWA and K. KATO 1997 *Cybernetics and Systems* **28**, 225–244. Application of wavelet transform to compression of mechanical vibration data.
25. M. J. DESFORGES, P. F. JACOB and J. E. COOPER 1998 *Proceedings of the Institution of Mechanical Engineers, Part C, Journal of Mechanical Engineering Science* **212**, 687–703. Applications of probability density estimation to the detection of abnormal conditions in engineering.
26. P. S. ADDISON 2002 *The Illustrated Wavelet Transform Handbook*. Bristol: The Institute of Physics Publishing.
27. W. CHEN, M. D. NOVAK, T. A. BLACK and X. LEE 1997 *Boundary-Layer Meteorology* **84**, 99–123. Coherent eddies and temperature structure functions for three contrasting surfaces. Part 1: ramp model with finite microfront time.
28. W. GAO and B. L. LI 1993 *Journal of Applied Meteorology* **32**, 1717–1725. Wavelet analysis of coherent structures at the atmosphere-forest interface.
29. C.-H. LU and D. R. FITZJARRALD 1994 *Boundary-Layer Meteorology* **69**, 43–69. Seasonal and diurnal variations of coherent structures over a deciduous forest.
30. I. DAUBECHIES 1992 Ten Lectures on Wavelets, *CBMS-NSF Regional Conference Series in Applied Mathematics*. Philadelphia: SIAM.
31. R. R. COIFMAN and D. L. DONOHO 1995 *Lecture Notes in Statistics* **103**, 125–150. Translation invariant de-noising.
32. N. DELPRAT, B. ESCUDIE, P. GUILLEMAIN, R. KROMLAND-MARTINET, P. TCHAMITCHAIN and B. TORRESANI 1992 *IEEE Transactions on Information Theory* **38**, 644–664. Asymptotic wavelet and Gabor analysis: extraction of instantaneous frequencies.
33. R. A. CARMONA, W. L. HWANG and B. TORRESANI 1997 *IEEE Transactions on Signal Processing* **45**, 2586–2590. Characterization of signals by the ridges of their wavelet transform.
34. R. A. CARMONA, W. L. HWANG and B. TORRESANI 1999 *IEEE Transactions on Signal Processing* **47**, 480–492. Multiridge detection and time–frequency reconstruction.
35. W. J. STASZEWSKI 1997 *Journal of Sound and Vibration* **203**, 283–305. Identification of damping in MDOF systems using time-scale decomposition.
36. W. J. STASZEWSKI 1998 *Journal of Sound and Vibration* **214**, 639–658. Identification of non-linear systems using multi-scale ridges and skeletons of the wavelet transform.
37. S. ROUX, J. F. MUZY and A. ARNEODO 1999 *The European Physical Journal B* **8**, 301–322. Detecting vorticity filaments using wavelet analysis: about the statistical contribution of vorticity filaments to intermittency in swirling turbulent flows.
38. J. S. SAHAMBI, S. M. TANDON and R. K. P. BHATT 1997 *IEEE Engineering in Medicine and Biology* **16**, 77–83. Using wavelet transforms for ECG characterization: an on-line digital signal processing system.
39. J. S. SAHAMBI, S. M. TANDON and R. K. P. BHATT 1997 *Medical and Biological Engineering and Computing* **35**, 747–751. Quantitative analysis of errors due to power-line interference and base-line drift in detection of onsets and offsets in ECG using wavelets.
40. B.-L. LI and C. LOEHLE 1995 *Geophysical Research Letters* **22**, 3123–3126. Wavelet analysis of mulitscale permeabilities in the subsurface.

41. S. KADAMBE, R. MURRAY and G. F. BOUDREAUX-BARTELS 1999 *IEEE Transactions on Biomedical Engineering* **46**, 838–848. Wavelet transform-based QRS complex detector.
42. L. M. BRUCE and R. R. ADHAMI 1999 *IEEE Transactions on Medical Imaging* **18**, 1170–1177. Classifying mammographic mass shapes using the wavelet transform modulus-maxima method.
43. R. A. CARMONA, W. L. HWANG and R. D. FROSTIG 1995 *IEEE Transactions on Medical Imaging* **14**, 556–564. Wavelet analysis for brain-function imaging.
44. M. HAASE and B. LEHLE 1998 in *Fractals and Beyond* (M. M. Novak, editor). Singapore: World Scientific. Tracing the skeleton of wavelet transform maxima lines for the characterization of fractal distributions,
45. M. E. DEGAUDENZI and C. M. ARIZMEDI 1999 *Physical Review E*, **59**, 6569–6573. Wavelet-based fractal analysis of airborne pollen.
46. S. D. MEYERS, B. G. KELLY and J. J. OBRIEN 1993 *Monthly Weather Review* **121**, 2858–2866. An introduction to wavelet analysis in oceanography and meteorology: with application to the dispersion of Yanai waves.
47. C. TORRENCE and G. P. COMPO 1998 *Bulletin of the American Meteorological Society* **79**, 61–78. A practical guide to wavelet analysis.
48. S.-H. LEE, H. ZAHOUANI, R. CATERINI and T. G. MATHIA 1998 *International Journal for Machine Tools Manufacture* **38**, 581–589. Morphological characterisation of engineered surfaces by wavelet transform.
49. S. GUILBAUD and B. AUDOIN 1999 *Journal of the Accoustical Society of America* **105**, 2226–2235. Measurement of the stiffness coefficients of a viscoelastic composite material with laser generated and detected ultrasound.
50. H. LI and T. NOZAKI 1995 *JSME International Journal*, *Series B* **38**, 525–531. Wavelet analysis for the plane turbulent jet.
51. P. S. ADDISON 1999 *Proceedings of I Mech E*, *Part C*, *Journal of Mechanical Engineering Science* **213**, 217–229. Wavelet analysis of the breakdown of a pulsed vortex flow.
52. P. S. ADDISON, K. B. MURRAY and J. N. WATSON 2001 *American Society of Civil Engineers*, *Journal of Engineering Mechanics* **127**, 58–70. Wavelet transform analysis of open channel wake flows.
53. H. HIGUCHI, J. LEWALLE and P. CRANE 1994 *Physics of Fluids* **6**, 297–305. On the structure of a two-dimensional wake behind a pair of flat plates.
54. G. IUSO, M. ONORATO and M. ONORATO (Jr.) 1996 *Advances in Turbulence* VI, *Proceedings of the Sixth European Turbulence Conference*, *Lausanne*, *Switzerland*, 2–5 *July* 1996 (S. Gavrilakis, L. Machiels and P. A. Monkewitz, editors), 519–520. Dodrecht: Kluwer Academic Publishers. Spectral analysis of near wall turbulent flow.
55. S. V. KAILAS and R. NARASHIMA 1999 *Experiments in Fluids* **27**, 167–174. The eduction of structures from flow imagery using wavelets. Part 1. The mixing layer.
56. S. COLLINEAU and Y. BRUNET 1993 *Boundary Layer Meteorology* **65**, 357–379. Detection of turbulent coherent motions in a forest canopy. Part 1: wavelet analysis.
57. S. COLLINEAU, Y. BRUNET 1993 *Boundary Layer Meteorology* **66**, 49–73. Detection of turbulent coherent motions in a forest canopy. Part 2: time-scales and conditional averages.
58. C. R. HAGELBERG, D. I. COOPER, C. L. WINTER and W. E. EICHINGER 1998 *Journal of Geophysical Research* **103**, 16 897–16 907. Scale Properties of microscale convection in the marine surface layer.
59. N. TAKEUCHI, K. I. NARITA and Y. GOTO 1994 *Journal of Geophysical Research* **99**, 10 751–10 757. Wavelet analysis of meteorological variables under winter thunderclouds over the Japan Sea.
60. P. SULLIVAN, R. ANCIMER and J. WALLACE 1999 *Experiments in Fluids* **27**, 92–101. Turbulence averaging within spark ignition engines.
61. S. MALLAT 1998 *A Wavelet Tour of Signal Processing*. San Diego: Academic Press.
62. M. J. TURNER 1996 *CIRIA Report R*144. London: Thomas Telford Press. The role of integrity and other non-destructive testing in the evaluation of piled foundations.
63. P. S. ADDISON, J. N. WATSON and A. SIBBALD 1999 13*th ASCE Engineering Mechanics Division Conference*, *Baltimore*, *MD*, *U.S.A.*, *June* 13–16. The practicalities of using wavelet transforms in the non-destructive testing of piles on CD.
64. J. N. WATSON 2001 *Ph.D. Thesis*, *Napier University*, *Edinburgh*. The Application of Neural Networks to Non-Destructive Testing Techniques.
65. J. LU, J. B. WEAVER, D. M. HEALY and Y. XU 1992 *Proceedings of the IEEE-SP International Symposium on Time–Frequency and Time-Scale Analysis*, *Victoria*, *BC*, *October*, 1992. Noise reduction with multiscale edge representation and perceptual criteria.

66. J. N. WATSON, P. S. ADDISON and A. SIBBALD 1999 *Journal of Shock and Vibration* **6**, 267–272. The de-noising of sonic echo test data through wavelet transform reconstruction.
67. J. N. WATSON, P. S. ADDISON, G. R. CLEGG, M. HOLZER, F. STERZ and C. E. ROBERTSON 2000 *Resuscitation* **43**, 121–127. Evaluation of arrythmic ECG signals using a novel wavelet transform method.
68. P. S. ADDISON, J. N. WATSON, G. R. CLEGG, M. HOLZER, F. STERZ and C. E. ROBERTSON 2000 *IEEE Engineering in Medicine and Biology* **19**, 383–392. A novel wavelet based analysis reveals hidden structure in ventricular fibrillation.

APPENDIX A

Let $F(\omega) = |\psi(\omega)|^2/\omega$, C_g of the mother complete Morlet wavelet is then

$$C_g = \int_0^\infty F(\omega)\,\mathrm{d}\omega = \int_0^\infty \frac{2\sqrt{\pi}\,\mathrm{e}^{-(\omega^2+\omega_o^2)}(\mathrm{e}^{\omega\omega_o}-1)^2}{\omega}\,\mathrm{d}\omega. \tag{A1}$$

The integral function $F(\omega)$ for all the values of ω_o has a finite area between $\omega = 0$ and ∞, which can be examined mathematically as follows.

As ω approaches zero, the integral function $F(\omega)$ becomes (0/0). By applying L'Hospital's Principle, the limit of the function will be zero as shown in the following deduction:

$$\lim_{\omega\to 0}\frac{2\sqrt{\pi}\,\mathrm{e}^{-(\omega^2+\omega_o^2)}(\mathrm{e}^{\omega\omega_o}-1)^2}{\omega} = \lim_{\omega\to 0} 4\sqrt{\pi}\,\frac{(\mathrm{e}^{\omega_o\omega}-1)(\omega+\omega_o-\omega\,\mathrm{e}^{\omega_o\omega})}{\mathrm{e}^{(\omega^2+\omega_o^2)}} = 0. \tag{A2}$$

This means the numerator is a higher ordered infinity of the denominator. Similarly, by applying the same principle, one can find that the limit of the function $F(\omega)$ is also zero, while ω approaches infinity:

$$\lim_{\omega\to\infty}\frac{2\sqrt{\pi}\,\mathrm{e}^{-(\omega^2+\omega_o^2)}(\mathrm{e}^{\omega\omega_o}-1)^2}{\varpi} = 0. \tag{A3}$$

By differentiating $F(\omega)$, we have the following expression:

$$\frac{\mathrm{d}F(\omega)}{\mathrm{d}\omega} = 2\sqrt{\pi}\,\frac{1}{\omega^2}\,\mathrm{e}^{-(\omega^2+\omega_o^2)}(\mathrm{e}^{\omega_o\omega}-1)[2\omega_o\omega-(\mathrm{e}^{\omega_o\omega}-1)(2\omega^2+1)]. \tag{A4}$$

Letting the right side equal to zero, two roots of the equation can be found as $\omega_1 = 0$, $\omega_2 = \infty$ and the third root ω_3 is the root of the transcendent equation given by

$$\omega_o\omega = \log\left(\frac{2\omega_o\omega}{2\omega^2+1}+1\right). \tag{A5}$$

Hence, the function $F(\omega)$ reaches its maximum once at $\omega = \omega_3$ somewhere in the region between $\omega = 0$ and $\omega = \infty$. This guarantees that C_g will have a single finite value for a complete Morlet mother wavelet and will be a single valued function of ω_o. It is difficult to find the analytical form of the integral of equation (A1). Instead, the values of C_g together with the passband centre of the wavelet transform, ω_c, can be computed using numerical integration, for example, for $\omega_o = 1, 2, 3, 4$ and 5, $C_g = 2{\cdot}036, 3{\cdot}152, 2{\cdot}228, 1{\cdot}625$ and $1{\cdot}284$, and $\omega_c = 1{\cdot}555, 2{\cdot}182, 3{\cdot}085, 4{\cdot}062$ and $5{\cdot}050$ respectively. It is interesting that C_g has its maximum around $\omega_o = 2$.

The energy spectrum of the standard Morlet mother wavelet is given as follows:

$$|\psi(\omega)|^2 = 2\sqrt{\pi}\,\mathrm{e}^{-(\omega-\omega_o)^2}. \tag{A6}$$

The admissibility constant, C_g, of the wavelet is given by the following integral:

$$C_g = \int_0^\infty F(\omega)\,\mathrm{d}\omega = \int_0^\infty \frac{2\sqrt{\pi}\,\mathrm{e}^{-(\omega-\omega_o)^2}}{\omega}\mathrm{d}\omega. \tag{A7}$$

As stated above, previous investigators used the central frequency, $\omega_o = 5$–6. The reason is obvious because, if $\omega_o < 5$, the energy spectrum of standard wavelet will be truncated by the vertical axis ($\omega = 0$) and the definition of C_g is violated. This can be seen quite clearly in Figure 1(c) and 1(d), as the singularity of the function $F(\omega)$ near $\omega = 0$ makes the integration inadequate while a converged C_g cannot be found. According to the nature of the function, $F(0)$ would never be zero. However, if ω_o is sufficiently large, while ω approaches zero, it is still possible to maintain the ratio of the numerator and denominator part of $F(\omega)$ as unity. The trend can be examined mathematically by looking at the limit given below:

$$\lim_{\omega\to 0,\ \omega_o\to\infty} \frac{2\sqrt{\pi}\,\mathrm{e}^{-(\omega-\omega_o)^2}}{\omega} = \lim_{\omega\to 0,\ \omega_o\to\infty} 2\sqrt{\pi}\,\frac{\mathrm{e}^{2\omega_o\omega}}{\omega\,\mathrm{e}^{(\omega^2+\omega_o^2)}}. \tag{A8}$$

The double limit above implies that while ω approaches zero, ω_o moves towards infinity in the opposite direction. When $\omega = \delta\omega_o$ $(0 < \delta \ll 1)$

$$\frac{\mathrm{e}^{2\delta\omega_o\omega}}{\delta\omega_o\,\mathrm{e}^{(\delta^2+1)\omega_o^2}} = 1. \tag{A9}$$

Taking logarithm on both sides one obtains

$$(\delta^2+1)\omega_o^2 - 2\omega_o\omega\delta + \log\delta\omega_o = 0. \tag{A10}$$

This is a transcendent equation which can only be solved numerically. However, for $0 < \delta \ll 1$, δ can be estimated by

$$\delta = \frac{\mathrm{e}^{-\omega_o^2}}{\omega_o}. \tag{A11}$$

For $\omega_o = 5$, δ and ω are as small as $0{\cdot}2\mathrm{e}^{-25} (= 2{\cdot}7776\times10^{-12})$ and e^{-25} $(= 1{\cdot}388\times10^{-11})$, respectively, which means the first discrete point will be extremely closer to zero. Hence, the use of $\omega_o \geqslant 5$ will avoid the singularity of function $F(\omega)$ and a single-valued C_g can be determined.

APPENDIX B

In this appendix we show that, for low values of central frequency, the real part of the complete Morlet wavelet takes the approximate form of the Mexican hat function. The complete Morlet is given as

$$\psi(t) = \frac{1}{\sqrt[4]{\pi}}(\mathrm{e}^{\mathrm{i}\omega_o t} - \mathrm{e}^{-\omega_o^2/2})\,\mathrm{e}^{-t^2/2}, \tag{B1}$$

which can be written as

$$\psi(t) = \frac{1}{\sqrt[4]{\pi}}(\cos\omega_o t + \mathrm{i}\sin\omega_o t - \mathrm{e}^{-\omega_o^2/2})\,\mathrm{e}^{-t^2/2}, \tag{B2}$$

the real part of which is

$$\mathrm{Re}\{\psi(t)\} = \frac{1}{\sqrt[4]{\pi}}(\cos \omega_o t - \mathrm{e}^{-\omega_o^2/2})\,\mathrm{e}^{-t^2/2}. \tag{B3}$$

We can expand the exponentional function as

$$\mathrm{e}^z = 1 + z + \frac{z^2}{2} + \frac{z^3}{6} + \cdots \tag{B4}$$

and the cosine function as

$$\cos z = \sum_{n=0}^{\infty} \frac{(-1)^n z^{2n}}{(2n)!} = 1 - \frac{z^2}{2} + \frac{z^4}{24} - \cdots. \tag{B5}$$

Incorporating these expansions into equation (B3), and expanding only the second order ω_0 terms, one arrives at

$$\mathrm{Re}\{\psi(t)\} = \frac{1}{\sqrt[4]{\pi}}\left(1 - \frac{(\omega_o t)^2}{2} - \left(1 + \left(-\frac{\omega_o^2}{2}\right)\right)\right)\mathrm{e}^{-t^2/2}, \tag{B6}$$

which reduces to

$$\mathrm{Re}\{\psi(t)\} = \frac{1}{\sqrt[4]{\pi}}\frac{\omega_o^2}{2}(1 - t^2)\,\mathrm{e}^{-t^2/2}, \tag{B7}$$

which has the same form as the Mexican hat function of equation (31) weighted by $(1/\sqrt[4]{\pi})\,\omega_o^2/2$. Figure B1 illustrates the Mexican hat-like shape of the complete Morlet wavelet at low central frequencies. In the figure, the Mexican hat wavelet of equation (31) is plotted against the real part of the complete Morlet wavelet, normalized by dividing it by

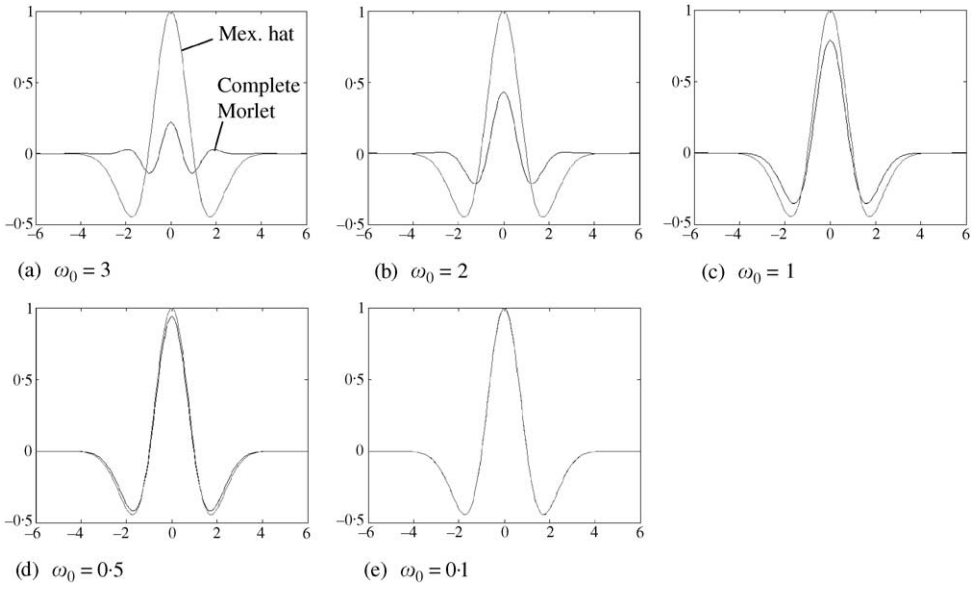

Figure B.1. The behaviour of the real part of the Morlet wavelet at small values of central frequency compared to the Mexican hat wavelet: (a) $\omega_0 = 3$, (b) $\omega_0 = 2$, (c) $\omega_0 = 1$, $\omega_0 = 0{\cdot}5$, (e) $\omega_0 = 0{\cdot}11$.

$(1/\sqrt[4]{\pi})\,\omega_o^2/2$. The adoption of the Mexican hat shape of the Morlet wavelet becomes obvious at low central frequencies. However, the complex part of the complete Morlet wavelet has no such correction term and hence dominates at very low values of ω_0. Current research by the authors therefore centres around the derivation of a Morlet-like wavelet without such limitations.